A Detailed Observation of the Nonprojectiveness of X-ray Moiré-Fringed Diffraction Images

J. YOSHIMURA

*Institute of Inorganic Synthesis, Faculty of Engineering, Yamanashi University, 4-3-11 Takeda, Kofu 400, Japan.
E-mail: yoshimur@rasa.miy.yamanashi.ac.jp*

Abstract

It has been shown in recent years that X-ray moiré fringes are not given exactly as a projection of the intensity pattern on the exit surface of the crystal but oscillate spatially along the beam path behind the crystal. Experiments to reveal the real state of this moiré image's nonprojectiveness have been conducted using synchrotron-radiation plane-wave topography, an Si bicrystal specimen and a simultaneous recording of moiré topographic images onto a set of multilayered X-ray films. This paper reports the following experimental results: intensity profiles revealing an unusual striking figure of the space wave field of moiré fringes; qualitative analysis of the fringe profile change in its manner of occurrence and in the effect on the fringe-position variation; plots of oscillating fringe position and fringe direction. The amplitudes of the fringe oscillation determined over the whole field of the moiré pattern exhibit a non-uniform characteristic distribution pattern that can be related to a specific feature of the intensity pattern on the specimen.

1. Introduction

Interference fringe patterns observed in X-ray topography have been considered as a projection of the intensity distribution on the exit surface of the crystal in the direction of the X-ray beam. It has been remarked in a review article by Kato (Azaroff *et al.*, 1974) that *Pendellösung* fringes should be a projective image in this sense. This projectiveness can be understood to be derived from the condition $|\mathbf{K}| = |\mathbf{K}'|$, *i.e.* $\Delta\mathbf{K} \perp \bar{\mathbf{K}}$, which commonly applies to all interferences between elastically scattered X-ray waves. Here, $\mathbf{K}$ and $\mathbf{K}'$ are the wave vectors of interfering waves in vacuum, $\Delta\mathbf{K} = \mathbf{K}' - \mathbf{K}$ and $\bar{\mathbf{K}} = \frac{1}{2}(\mathbf{K} + \mathbf{K}')$.

In recent papers (Yoshimura, 1987, 1989; Yoshimura & Ishikawa, 1990; Yoshimura, 1991a, 1992), however, it has been shown that moiré interference fringes vary their positions and directions with the observation points along the beam path and thus are not exactly the projection even though they may approximate it. Fringe positions and directions viewed locally in the moiré pattern vary considerably, although the global fringe

pattern does not vary appreciably. These variations of moiré fringes do not exceed a small limit except for a special case (see §3.1) and the fringes repeat a spatial oscillation within this amplitude. Such a deviation from the picture projectiveness has been called nonprojectiveness (NPJ). An explanation for the NPJ is difficult to find in the understanding of moiré fringes, which requires that the moiré image should be exactly the projection. To show this clearly, a theoretical description of X-ray moiré fringes according to the conventional understanding is briefly given in Appendix *A*.

From investigations so far, it seems that NPJ is an essential nature of moiré fringes and is quite a new phenomenon inexplicable by any known effects. In this paper, we present some detailed experimental facts on moiré fringes' NPJ, obtained from recent experiments and experimental data analysis. Characteristics of the NPJ will be clarified to a certain extent in this report.

2. Experimental procedure

2.1. Recording of simultaneous moiré topographs

The experiment was conducted using synchrotron radiation at Station BL-15C at the Photon Factory, KEK, Japan. The experimental set-up is illustrated in Fig. 1. X-rays from the synchrotron source were monochromatized and collimated by an Si(111) premonochromator and a collimator of Si 220 asymmetric reflection with asymmetry factor $b = 1/40$. The wavelength of the incident X-rays onto the specimen was centered at $\lambda_o = 0.72$ Å with the spread $\Delta\lambda/\lambda_o \simeq 10^{-3}$. The angular spread was 0.08″ for individual wavelengths and 0.34″ in the whole wavelength range (Appendix *B*). The specimen was a monolithic Si bicrystal. The 220 reflection was used in the symmetric Laue geometry, the specimen being aligned in the parallel setting with the upstream Si(220) collimator.

Details of the specimen are as shown in Fig. 1(*b*). Besides the interspacing gap between the two component crystals, a cut parallel to the *xz* plane was incised to ease the rotation about the *z* axis. The thicknesses of the front and rear crystals and the gap were 1.615, 1.510 and 0.225 mm, respectively, the total thickness being 3.35 mm. The reciprocal-lattice-vector difference $\Delta\mathbf{g}$ to

produce moiré fringes was introduced largely by a minute relative rotation between the two component crystals about a horizontal axis (z axis), which occurred unforcedly because of the mass difference between the two. The magnitude of rotation is estimated to be $\sim 4 \times 10^{-7}$ rad from the fringe spacing. Furthermore, the rear crystal was pulled at a point on its edge by a weight (denoted by L) of 0.0–0.3 g, so as to rotate about the goniometer axis (y axis). This rotation, though not measured, is estimated to be 2×10^{-7}–2×10^{-6} rad g^{-1} according to elasticity theory.

Plane-wave diffraction images each produced in the way above with an accompanying moiré pattern were recorded simultaneously onto a set of 8–12 X-ray films placed parallel with a constant interval. The specimen was then set at the peak position of the rocking curve of the diffracted beam. Very thin (20 µm) Pt wires stretched in a rigid frame were placed between the specimen and the X-ray films so that their shadow images made a reference for position and/or orientation on the topographs. The specimen-to-film distance, z_d, was 54–64 mm (except for one recording run) and the film-to-film separation, Δz_d, was 0.0–0.98 mm. The transmitted and diffracted beams (O and G beams, respectively) were incident on the X-ray films, making angles of 2.3 and 19.3°, respectively, to the normal to the film plane.
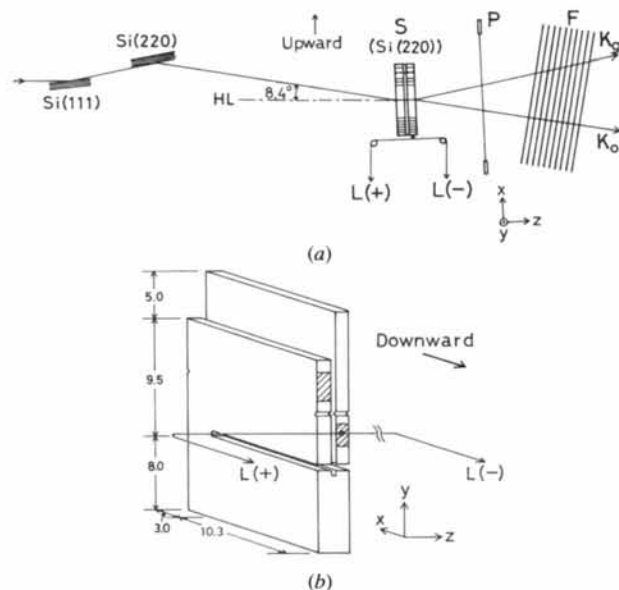
Exposure time was 25–35 s. Single-coated X-ray films were specially prepared from conventional-type high-resolution X-ray films (Fuji no. 50; undeveloped grain size 0.3 µm) for this moiré-image recording. The emulsion thickness was 10 µm. The intensity attenuation of X-rays due to film absorption was 6.7% a film. The moiré-image recording was repeated with different pulling loads L and different mean film intervals $\overline{\Delta z_d}$. The film orientation and z_d were determined after the experiment by measuring the distances between point-like defect images (indicated with letters A and C in Fig. 2) in the O- and G-beam topographs.

Rocking curves were measured to check lattice distortion in the specimen. Those measured from a 1.0 (x direction) $\times$ 0.3 mm (y direction) area and a stripe 10.0×0.3 mm on the specimen exhibited half-widths (FWHM) of 1.42 and 1.61″, respectively, when $L = 0$. The half-width of the calculated rocking curve for the assumed strain-free $\Delta \mathbf{g} = 0$ state is 1.44″. The rocking-curve measurement indicates that the specimen was free of heavy strain but a weak strain that gives an angular broadening of 0.2″ was present.

2.2. Image processing of moiré topographs

The photographic density, D, of the moiré topographs obtained was examined by a microphotometer. The microphotometric measurement showed that the D value is 0.15–1.05 with a fog density of 0.15–0.16 through all the data films of this experiment. This density range is in the toe region in the D–E characteristic curve. The experiment was performed to reveal the exact D–E curve

Fig. 1. (a) General view of the experimental set-up. S specimen; P thin Pt wire stretched in a rigid frame; F X-ray films; $L(+)$ and $L(-)$ load for causing the rear crystal to rotate about the y axis [(+, −) give the sign of the load]. x axis ∥ [1$\bar{1}$0], y axis ∥ [11$\bar{2}$], z axis ∥ [111]. The x and z axes lie in the vertical plane and the dashed line HL indicates the horizontal direction. (b) Detailed drawing of the specimen bicrystal. Dimensions are given in mm. Adhesive (araldite) was painted on the hatched portion to fix the pulling wire and to attach a balancer for adjusting the mass difference between the two component crystals.
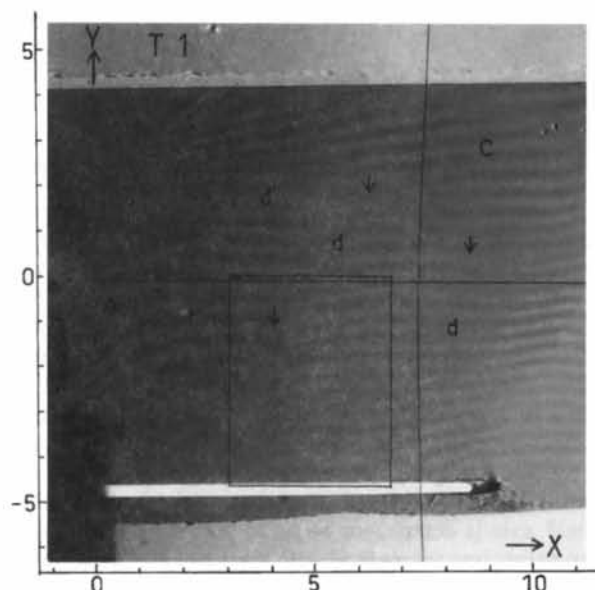

Fig. 2. An example of an experimental moiré topograph. T set no. 8, T1 topograph. O-beam image. The diffraction vector is from left to right in the topograph. For details see text.

of the single-coated X-ray films used, and a good linearity of the $D–E$ characteristic was confirmed (Appendix C).

Moiré topographs were processed by an image processor (PIAS LA-525) with 256 gray levels. The image on the X-ray films was input into the processor with linear presetting, using an optical system. One pixel length in input images corresponds to ca 20 μm on the real scale. These original input images received shading correction, gray-level reversal, dynamic range expansion and smoothing. The gray-level reversal means the transformation $I(X,Y) \rightarrow [255 - I(X,Y)]$, $I(X,Y)$ being the gray level or the image intensity at a point (X,Y). The smoothing was made with an appropriate space filter such as a 3×3 matrix. Additionally, use of the image processor offered another way of determining the D value to make the D measurement possible at any site in the moiré topographs (Appendix C).

The magnitude of the oscillatory density variations of moiré fringes above the background density was less than 0.15 in D value through all the data topographs. The relative drop from linearity of the image intensity vs density curve was 15.3% for this limiting D value (Appendix C). Fringe profiles taken from processor images are compressed by this amount at the maximum, compared with the corresponding density profiles. The relationship with the real wave-field intensity can be considered in the same way. In practice, comparison of many examples showed that intensity profiles from processor images and density profiles taken by the microphotometer and the image processor agree well with each other, though not in the strict sense. The nonlinearity mentioned does not matter in discussing experimental results.

3. Experimental results

3.1. NPJ observed in simultaneous moiré topographs

First, we describe how to treat the moiré images and their common features. Fig. 2 shows one of a set of ten topographs taken simultaneously under the condition $L = +0.2\,\text{g}$ and the mean film interval $\overline{\Delta z_d} = 0.42\,\text{mm}$. The coordinates (X, Y) are taken on the image plane of the topographs, corresponding to the (x, y) coordinates on the specimen (Fig. 1). The X axis lies on the horizontal black line seen at medium height. This and the crossing vertical lines are the shadows of the Pt lines placed between the specimen and the recording films (the bending of the vertical line is due to the bent Pt wire). The Y axis is determined so as to pass on a small point-like defect image (marked with the letter A). Scale values on the X coordinate indicate 0.94 times the real length so as to correspond to the scale on the G-beam image (see §2.1; the scale on the G image was taken accidentally as the standard). The scale along the Y axis indicates the real

length. The sense of image contrast is taken so that white contrast indicates higher intensity.* Thus, the peak of the intensity oscillation of the fringe pattern lies on a line of white contrast. Sets of simultaneous topographs are called T sets. Member topographs of a T set are numbered in increasing order of z_d, as $T1$, $T2$ etc. Moiré fringes are numbered from the bottom on the moiré pattern, as fringe 1, fringe 2 etc.

As seen in Fig. 2, the fringe direction and spacing viewed globally are nearly constant within the moiré pattern except near the left edge. In the case of this T set, the fringe spacing is 0.30–0.45 mm and the fringe direction is inclined by 3–12° from the X axis. The fringe pattern is nearly a rotation moiré pattern. The fringe contrast is estimated as 0.12 at the maximum and takes various values from this to zero. Here, the contrast is defined by $(D_t - D_b)/(D_t + D_b)$, D_t and D_b being the top and bottom D values of the fringe profile. The fringe pattern near the left edge $(X < 2)$ is disturbed owing to lattice distortion caused by adhesive painted on the side surface of the specimen for experimental reasons. The characteristics of the global fringe pattern in other T sets are nearly the same as above but the fringe direction varies considerably with load L and fringe spacing also varies a little. Additionally, at positions indicated by short arrows, the number of fringes changes discontinuously by one. Although this feature is not treated in this paper, it should be noted that the discontinuities are of unknown nature, being different from a moiré dislocation† [for moiré dislocations, see Lang (1968) and Hart (1972)]. The present specimen contains no dislocations. Black elongated spots denoted by the letter d are ghost images from point-like defects in the collimator crystal [see Ishikawa (1990); not all spots are marked].

Fig. 3 compares moiré images on the simultaneous topographs of this T set in the rectangular area shown in Fig. 2. A striking change in the fringe pattern is noticed at first sight in fringes 1 and 2 in the space between lines a and b and lines b and c on Fig. 3. In fringe 1 between lines b and c, for instance, the fringe direction oscillates between upward to the left and nearly horizontal in the successive simultaneous topographs. The magnitude of the slope of fringe 2 varies in the topographs also in an alternating manner. On visual inspection, the change in the fringe direction is more easily recognizable than that in the fringe position, although the two changes occur together. It may be added that the intensity patterns of fringe 1 in $T3$, $T6$ and $T8$, although alike, are not exactly the same as each other. A similar comment may be made for fringe 1 in $T5$, $T7$ and $T10$. The repetition of the

---

* In the present author's view, this sense of contrast seems more suitable than the reverse one as far as this study is concerned because small intensity variations can be noticed more easily.

† This can be seen from the fact that the number and position of the discontinuity change between the O- and G-beam images and with moiré patterns for different values of L.

fringe pattern is in an approximate sense. Noticeable fringe-pattern variations are also found in fringes 5 and 6 between lines *a* and *b*, fringes 8–10 between lines *b* and *c* and fringes 1, 2, 6 and 7 between line *c* and the right edge. On the local scale, the fringe position and direction fluctuate everywhere in the fringe pattern.

The fringe pattern becomes obscure in the band area located in the upper-left portion indicated by arrows (in *T*3). The pattern has not only low contrast but is distorted in a complicated manner. Moreover, the fringe line continuation is partially or almost broken and the topology of the continuation of fringes is ambiguous and changing in the simultaneous topographs (see topographs from such a direction where fringes are arranged vertically). Such an obscurely patterned area is called non well defined fringe pattern area (NWD area) in this paper. In contrast to this, areas with unambiguous fringe patterns other than NWD areas are called well defined area (WD area). The NWD band area above is part of a long curved band in the whole field of the topograph (Fig. 2; see also Fig. 9). The occurrence of some low fringe-contrast bands like this, which are not always a

NWD area, is a common feature of this study's moiré topographs.

3.2. *NPJ observed in intensity profiles of fringes*

Fig. 4 shows three-dimensional intensity profiles output from the image processor for two of the moiré topographs in Fig. 3. The intensity profiles reveal the vacuum-space wave field in which the nonprojective fringe pattern was formed. The variations of fringes 1, 2 *etc.* observed in Fig. 3 can be verified satisfactorily by following the tops in the profile train along the fringes. It is remarkable that fringe profiles have very irregular shapes with fine substructures and have quite different shapes in the two topographs. It is also worth noting that fringe profiles vary between adjacent fringes and vary along each individual fringe within one topograph. Regarding the variation along individual fringes, some continuity or coherence seen in the partially continuous variation should also be noted. Additionally, on the right-hand side of the drops along the line $Y = 0$, the intensity
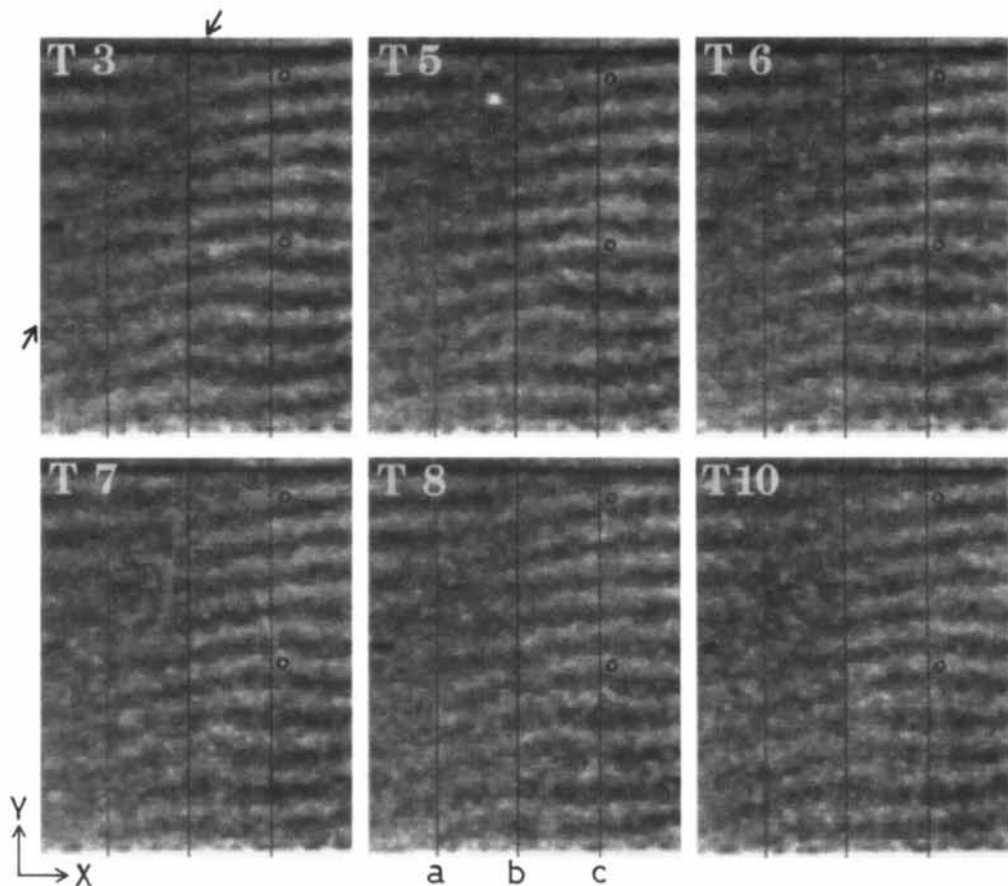

Fig. 3. Comparison of simultaneous moiré topographs. The same *T* set as Fig. 2. The specimen-to-film distance of the *T*1 topograph (Fig. 2) was $z_d = 55.1$ mm and the mean film interval between consecutively numbered topographs was $\overline{\Delta z_d} = 0.42$ mm. For ease of inspection, vertical lines are drawn at (*a*) $X = 4.0$, (*b*) $X = 5.0$ and (*c*) $X = 6.0$ mm. Fringes 5 and 10 are marked with small circles.
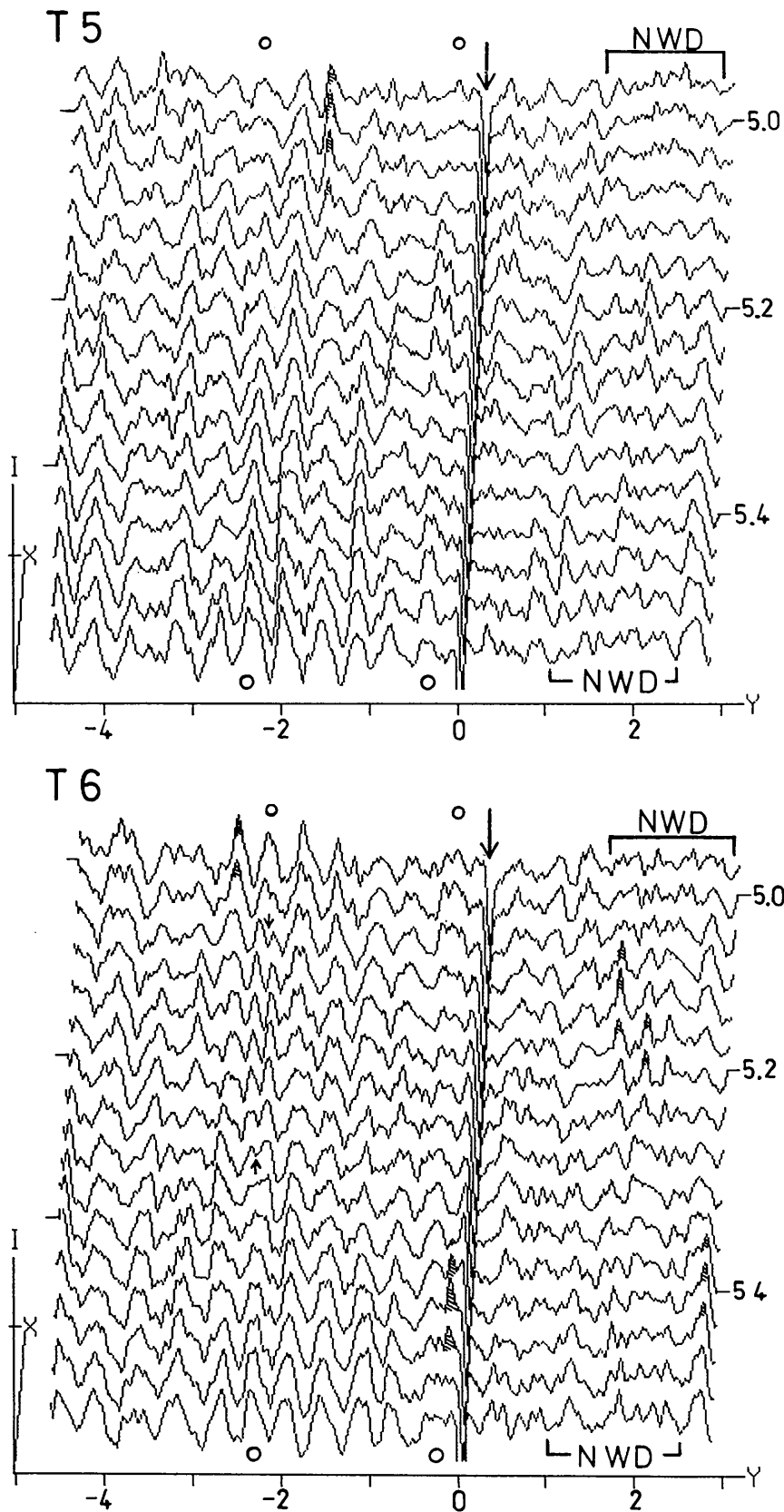
Fig. 4. Three-dimensional intensity profiles for the moiré topographs in Fig. 3. Numerical values on the right edge give the X coordinate. Small circles at the top and the bottom mark fringes 5 and 10. The abrupt drop along the line $Y = 0$ shows the Pt-line shadow. The hatching drawn in fringe 7 in $T5$, fringe 4 in $T6$ etc. shows noise arising from a blur or a scratch etc. in the recording film. An unusually large drop seen between the two arrows in fringe 5, $T6$, also seems to be caused by noise with unidentified origin.

profiles are shown of a NWD area located above the rectangular area in Fig. 2.

Fig. 5 compares intensity profiles on all the simultaneous topographs of the T set under study.* Profiles at a site of moderate variation are presented instead of those for large irregular variation. Fringe-profile variations occurring along the beam path can be observed fully in this form of display. Regarding the peak heights of profiles, those of three neighboring fringes (60 pixels) at least can be compared with a good accuracy. Peak heights between mutually distant fringes and on different topographs could not be compared exactly on account of processes in the film development and image processing. Fringes showing the largest and the smallest peak-position shifts are marked by □ and ⊙, respectively. Fringes showing large variation continue generally to have large variations throughout the entire path from $T1$ to $T10$ and fringes showing small variations similarly repeat only small variations.

Before observing the profile change in detail, we remark on some features of the fringe profile shape (see also Fig. 4): (a) Profile shapes generally are irregular and asymmetric, deviating greatly from the regular sinusoidal shape expected theoretically. It should also be noted that symmetric profiles in different shapes appear in small proportion (e.g. fringe 13 in $T3$, fringes 9 and 10 in $T10$). (b) In addition to single-peaked profiles, profiles having double- or more multiple-peaked tops are formed (e.g. fringes 6, 10 and 20 in $T3$; fringes 10 and 20 in $T10$). Besides the top, the profiles have subpeaks on their flanks and tails. The occurrence of such fine-structured profiles also features the present moiré fringes. (c) In the middle of two profile trains, a subsidiary peak train bridging the two main fringes appears occasionally. This is, for example, seen between fringes 2 and 3 in Fig. 4. The subpeak train may properly be regarded as an intermediate subfringe, not belonging to either main fringe.

The fringe profile variation of successive topographs in the T set are observed to occur at the following points:

* Comments are added on the accuracy of the profiles. Although accidental noise (blurs in data films) is not low, there is no ubiquitous background noise in this measurement. Therefore, the information on the wave-field intensity read by the image processor generally ought to have the accuracy of one gray scale, aside from the counting linearity of the CCD detector used. The rippled profile shapes also seen in Fig. 4 are not due to error noises but are of the wave field's own (this point is not discussed in the present paper in view of the length of the paper). The intensity of the original input images are modified by the shading correction. The leveling of the background intensity may be regarded as a proper image-analyzing procedure, even if it changes the apparent slopes of oscillatory intensity profiles. It should be noted that the peak and bottom positions (Y coordinate) of the profiles do not change except for some limited cases. Other distortions of profile shapes with this correction are undiscernably small. Smoothing is also a proper data processing and does not change the approximate shapes of the profiles. In conclusion, the fringe profiles in Fig. 5 are presented giving their fine structures with negligibly small error, though the intensity scale is arbitrary and the nonlinearity mentioned in §2.2 should be remembered.

(a) Variation in the shape asymmetry. For example, the profile shape of fringe 20 varies alternately between left-inclined shapes ($T1$, $T2$, $T4$, $T5$, $T7$, $T10$) and right-inclined or nearly symmetric shapes ($T3$, $T6$, $T8$). Similar alternating variations of the shape-asymmetry direction are observed in fringes 1, 4, 12, 13 etc. Despite complications in the fringe profiles, we can see that such shape-asymmetry change occurs basically in all the fringes.

(b) Displacement of the profile bottom. Noticeable displacements of the bottom position are also seen in fringe 20. The basal displacement in general occurs together with the variations of shape asymmetry and of profile width. As is well shown in the example mentioned, either of the two feet of the profile makes a large displacement to the direction opposite to the profile shape's inclination.

(c) Variation in profile width. A good example is found in fringes 2 and 3 on the path from $T1$ to $T4$. The profile width of the two fringes oscillates on this partial path, and that with a kind of complementarity. The alternating width variations of the two fringes with the seeming complementarity continue to $T10$, though less regularly and markedly from $T5$ on.

(d) Variation in peak height. A comparatively good example is seen in a relative peak-height variation between fringes 13 and 14. Marked peak-height variations besides this is observed in fringes 2, 3, 10, 17 etc. This variation also proceeds in an oscillatory manner. Another better example is shown in Fig. 6. To show peak-height variations exactly, fringe profiles are given in the density scale in this figure. Fringes 14–25 are observed to repeat 1 to 4 cycles of peak-height oscillations in the path length 2.0 mm from $T1$ to $T12$.

(e) Variation in the fine structure (subpeaks) of profile. These elementary variations are found quite commonly in moiré topographs of this experiment. The displacement of the peak position, which can roughly be regarded as the same with the displacement of the fringe position, results from variations of (a) and (b). The relation between the two variations, i.e. the shape-asymmetry variation and the basal displacement, qualitatively is well illustrated in fringe 20. The two variations in general contribute to the peak shift not additively but subtractively. The shape-asymmetry variation is the primary contribution in most fringes. The basal displacement makes a secondary but appreciable contribution. The resulting peak shift mostly proceeds following the shape-asymmetry variation.

A further remark is made on a partial regularity seen in almost irregularly varying fringe profiles. In some fringes, profiles similar to the one in a front position (z_{d1}) appear repeatedly at rear positions (z_{d2}; $z_{d1} < z_{d2}$) more than one film interval (Δz_d) behind, with different profiles formed on the interspacing beam path. This is approximately the case with recurrences in fringe 20 as $T1 \rightarrow T5$, $T2 \rightarrow T7$ and $T3 \rightarrow T8$. Appreciable resem-

blance is seen in the shape asymmetry, width and fine structure of the repeated fringe profiles. Similar but less complete recurrences are seen also in fringes 1, 3 *etc.* Though enough good examples are found in Fig. 5, such meaningful repetitions were generally observed in fringe profiles of this experiment. Additionally, rear profiles do not recur in exactly the same shape as the front one, receiving necessarily some deformation. The profiles of
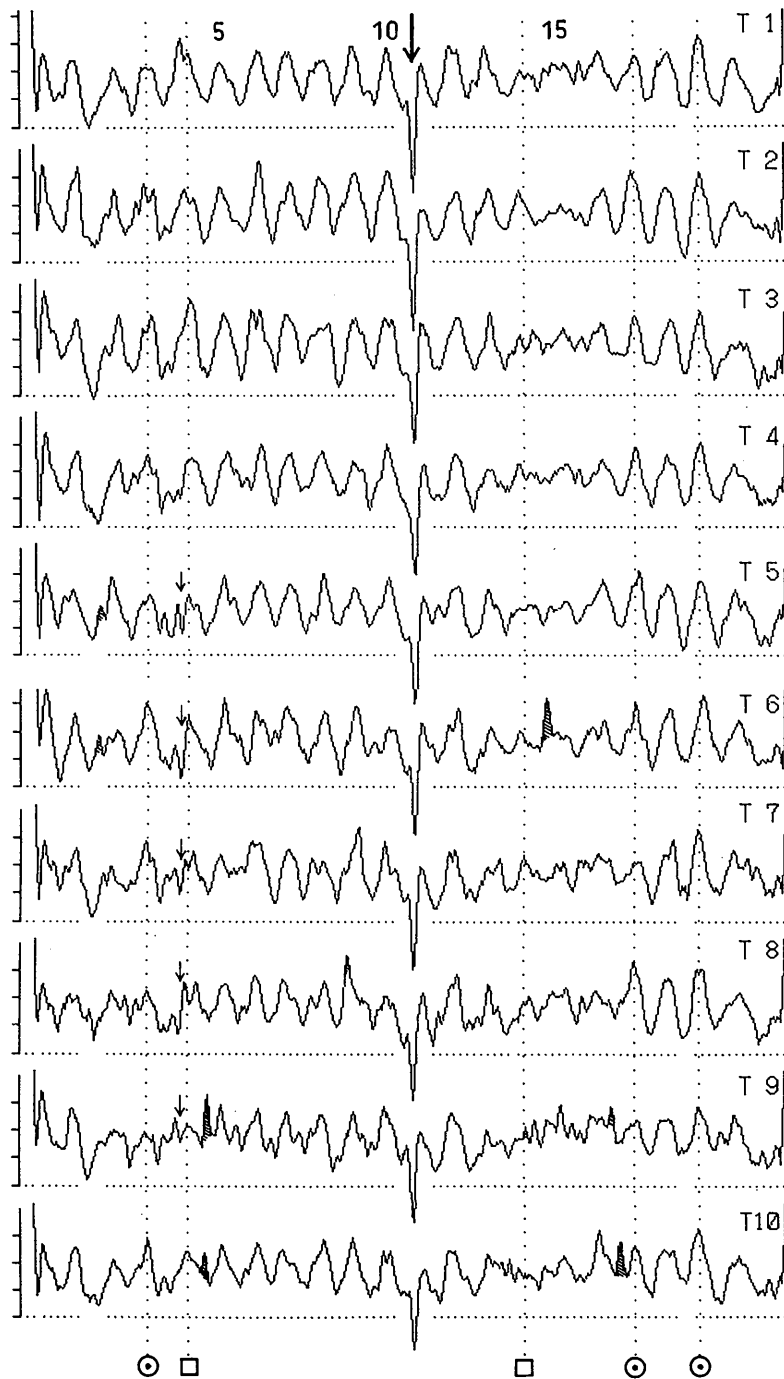

Fig. 5. Intensity profiles of moiré fringes viewed in the all-member topographs of the T set. T set no. 8, O-beam image. Taken by scan on the line $X = 6.0$ (line c in Fig. 3). Numerals at the top give fringe numbers. The bold arrow indicates the Pt-line shadow. Besides noises indicated by hatching, deep dips marked by thin arrows in fringe 4 also show a noise that probably arose from an absorbing particle sticking accidentally to the film of the $T4$ or $T5$ topograph.

more than a few fringes are repeated with some good resemblance up to one cycle of repetition, but few fringe profiles are repeated to the second cycle keeping good resemblance.

3.3. *Determination of the fringe position and direction*

It is not a simple problem to determine quantitatively observed complicated variations of the wave field. As the first step of characterization, we determined fringe positions in the varying fringe pattern. In this processing, information on the peak-height variation is not taken into account. Fringe positions (Y coordinate) were determined from fringe profiles, which were measured at successive X positions in the fringe pattern with an appropriate spacing. The fringe position was defined as the midpoint on the profile width at r times the peak height, r being between 1.0 and 0.35 (mainly 0.85 and 0.70). The peak height was determined as the height of the profile measured from an assumed smoothly varying back-

ground curve passing through the bottoms of the fringe profiles. The slope angle of the fringes was calculated by $\alpha_M = \tan^{-1}[(Y_1 - Y_2)/(X_1 - X_2)]$ from fringe positions thus determined, where (X_1, Y_1) and (X_2, Y_2) are the coordinates of the relevant two points.

Fig. 7 shows the result of the fringe-position determination for the fringe profiles shown in Fig. 5. Fringe positions obtained for $r = 0.85$ are plotted with vertical bars to show the variability with the r factor. The oscillations of fringe profiles are expressed in this graph. Such oscillatory plots were obtained from any T set recorded at any distance from the specimen. In this experiment, the occurrence of the fringe oscillation was confirmed up to the distance $z_d \simeq 200$ mm. This fact is considered to show that spatial oscillations of moiré fringes continue endlessly on the beam path. The cycle length of oscillations is not definable with enough clarity because of the irregular character of the oscillations. Nevertheless, from the inspection of many sample data including Fig. 7, we can comment on the general
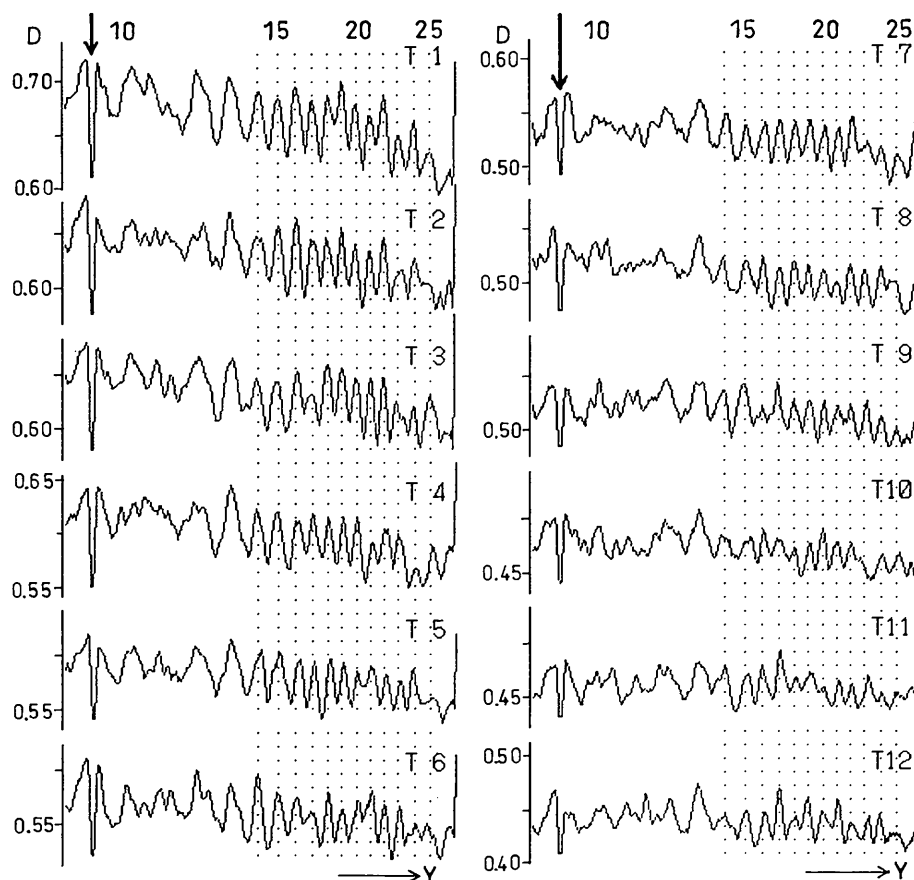

Fig. 6. Densitometric profiles of moiré fringes showing marked peak-height oscillations in simultaneous topographs. T set no. 16, O-beam image. Taken by scan on the line $X = 1.2$. For the $T1$ topographs, $z_d = 55.2$ mm, and the mean film interval was $\overline{\Delta z_d} = 0.18$ mm. D values of the topographs were obtained using the image-processor method (Appendix C). The synthesized D-value images were processed for dynamic range expansion and smoothing. The errors due to the incident illuminance fluctuation and digitizing are less than 0.01. The non-uniform illuminance coupled with the insufficient counting linearity of the CCD detector would add some error. The conditions of developing the films were not carefully unified.

characteristics of the cycle length as follows: (a) Through ten simultaneous topographs ($\overline{\Delta z_d} \simeq 0.4$ mm) on the entire path length of ca 4 mm, approximately two cycles of oscillation are repeated in general (see fringes 1, 4, 13 in Fig. 7); (b) In a small proportion of fringes, three cycles of oscillation are observed (fringes 2, 20); (c) In the neighborhood of a NWD area, three to four cycles of oscillation are occasionally found (fringe 14).

The oscillation amplitude a_M was determined from the variance of plots, σ, according to a formula $a_M = 2^{1/2}\sigma$. This relationship applies exactly to the case of a sinusoidal curve. Oscillation amplitudes thus determined

are considered to be a good measure of the irregularly fluctuating moiré wave field. In Fig. 7, oscillation ranges $\pm a_M$ of the respective fringes are indicated on the right edge. The amplitudes are 1.3 (fringes 1, 3, 17) to 4.6 (fringe 14) pixels and 6 to 22% for a_M/Λ, where Λ is the fringe spacing. Amplitudes generally were in the range $a_M/\Lambda = 0$–30% in T sets of the present experiment. It is seen from the observation in Fig. 5 that even a fringe that is assigned $a_M \simeq 0$ makes some oscillations at the level of the intensity profile.

An example of the fringe-slope determination is shown in Fig. 8, corresponding to the observation of the simultaneous topographs in Fig. 3. Each successive plot approximates well the continuous variation of the relevant fringe, although the lines only show that the plots refer to identical fringes. The fringe slope plots agree satisfactorily with visual inspection in Fig. 3, although the impression of some disagreement remains owing to such factors as the sensitiveness of the instrumental analysis to profile irregularities. The oscillation range is ± 3.5 to $\pm 6.4°$ from the mean values. Furthermore, fringes 2 and 3 in the interval $X = 4.2$–5.0 appear to show an in-phase oscillation. The oscillation of the two fringes appears to proceed independently of the oscillation of the adjacent two fringes 4 and 5. When viewed in the whole T set as in this graph, fringes 1 and 2 in $X = 5.0$–5.8 oscillate in a different manner. Apparent correlative oscillations of a few neighboring fringes as above were found generally at some frequency.
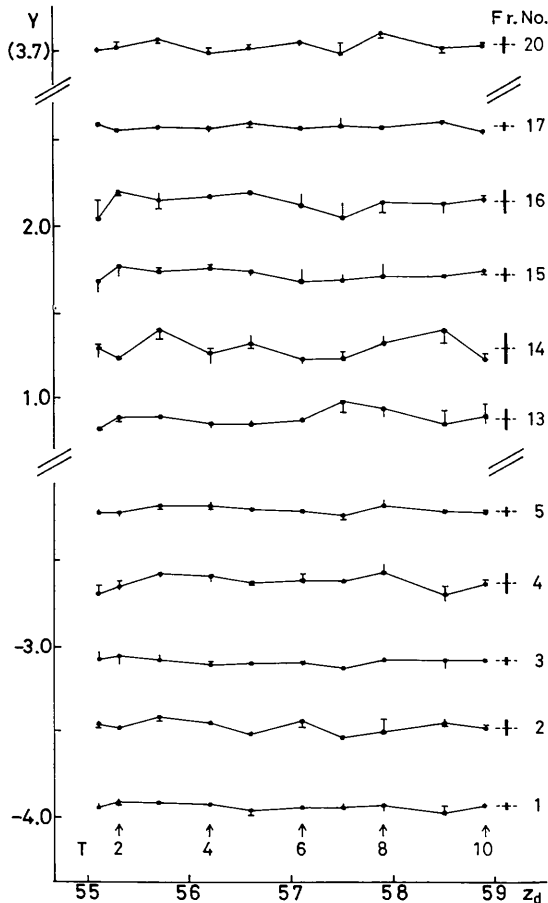
3.4. Amplitude map of fringe oscillation

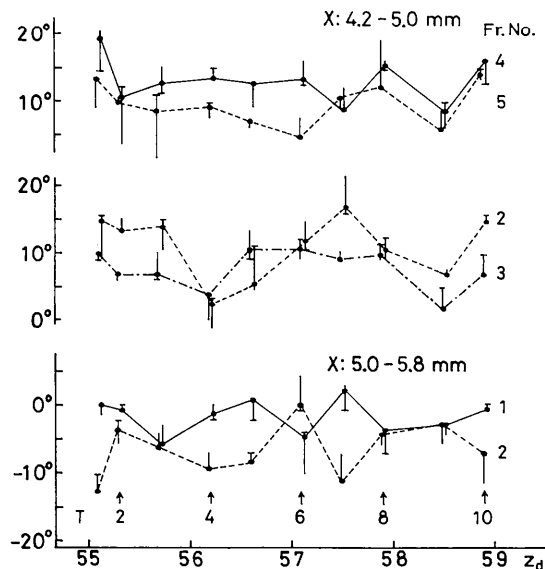Amplitudes of fringe oscillation vary with fringes as shown in Fig. 7. Although it is not clear there, many

Fig. 7. Plots of fringe position (Y) vs z_d. T set no. 8, O-beam image. Measured on the line $X = 6.0$. Y and z_d are given in mm. Numerals on the right edge give fringe numbers. Numerals below the plots of fringe 1 indicate the relevant topographs. Vertical bars attached to the plots indicate the variability of the determined fringe position with the r factor between $r = 0.7$ (T-shaped end) and $r = 1.0$ (opposite end). Either bar end coincides with the plotted point for $r = 0.85$ at many plots and some of the bars are too short to show in the figure. These bars may be regarded as an analog of error bars for assessing the correctness of the obtained fringe positions with $r = 0.85$. The determinations with individual r values have the accuracy of $|\Delta Y| < 1$ in pixels, estimated from the accuracy of the reference line and points, although they are affected significantly by irregularities in the profile shape.

Fig. 8. Plots of the slope angle α_M vs z_d. T set no. 8, O-beam image. Vertical bars have the same meaning as in Fig. 7.

other graphs of fringe oscillation (not shown) suggest that the amplitudes have a dependence on the location of fringes within the fringe pattern. To clarify fully the suggested location dependence, we performed the determination of the oscillation amplitudes in the fringe position over almost the whole area of the fringe pattern. The method of determination was as described for Fig. 7. The result for the T set treated in this paper is shown in Fig. 9(a). In this map, determined amplitudes are indicated by short vertical lines drawn in the range $\pm a_M$ centered at the mean fringe position. Thick vertical lines are drawn to indicate NWD areas in which the amplitude determination was unperformable. P and D indicate sites at which fringe positions were not determined correctly because of disturbances in the fringe profile coming from the Pt-line shadows and point-like defect images, respectively.

Remarks on this amplitude map are as follows:

(a) The map shows that the amplitude is not distributed completely randomly but is really distributed with an areal-scaled non-uniformity showing a location dependence. An auxiliary contour map in Fig. 9(b), giving a demarcation between large- and small-amplitude areas, makes this feature clearer. The amplitude distribution pattern of this T set is relatively indistinct and complicated. Viewed roughly, the point of the contour map can be summarized to be an alternating arrangement of the large- and small-amplitude bands; the large-amplitude bands are connected by a corridor in the upper region. The mean repeating interval of the band areas is about 4.2 mm in the X direction. It is confirmed that the amplitude map with $r = 0.70$ agrees well with Fig. 9(a) in its graphical features, but with a reduction in the distributed amplitudes. Additionally, large and small amplitudes are distributed in a partially scattered manner

in the areas from $L2$ to $S3$. This scatter makes the demarcation between the large- and small-amplitude bands indistinct. The repeated amplitude determination allows us to state that the scatter is of intrinsic origin, not arising from the determination procedure. This seems to show another regularity besides the location dependence mentioned.

(b) In most cases, a NWD area appears in the core of large-amplitude bands. It should be noted in Fig. 9(a) that amplitudes in the surrounding area increase towards the NWD area in a continuous manner. The limiting amplitude between the WD and NWD areas is generally 5–7 pixels, 25–33% for a_M/Λ. From the amplitude variation like this plus the topographic observation in Fig. 3, it may be presumed that the fringe oscillation in WD areas and the occurrence of NWD areas are of the same origin; the latter shows the extremal state of the former. Band $L3$ in Fig. 9(b) is interpreted to be an area where fringe oscillations are not amplified greatly enough to reach this extremity.

(c) The arrangement of large- and small-amplitude bands in the amplitude map agrees closely with the arrangement of the low-fringe-contrast and the normal-fringe-contrast areas in the moiré topographs in Fig. 2. This agreement is confirmable even for the large-amplitude band $L3$ not including a NWD area. The corresponding fringe-contrast reduction can be seen around $X = 9$ in the topograph. The presence of the low-contrast bands is a feature of the topograph as an approximate projection of the intensity pattern on the specimen. The agreement above proves the existence of a connection between the intensity pattern on the specimen and the fringe oscillation in the space wave field apart from the specimen. It may be added as experimental results, though not evidenced here, that the band pattern
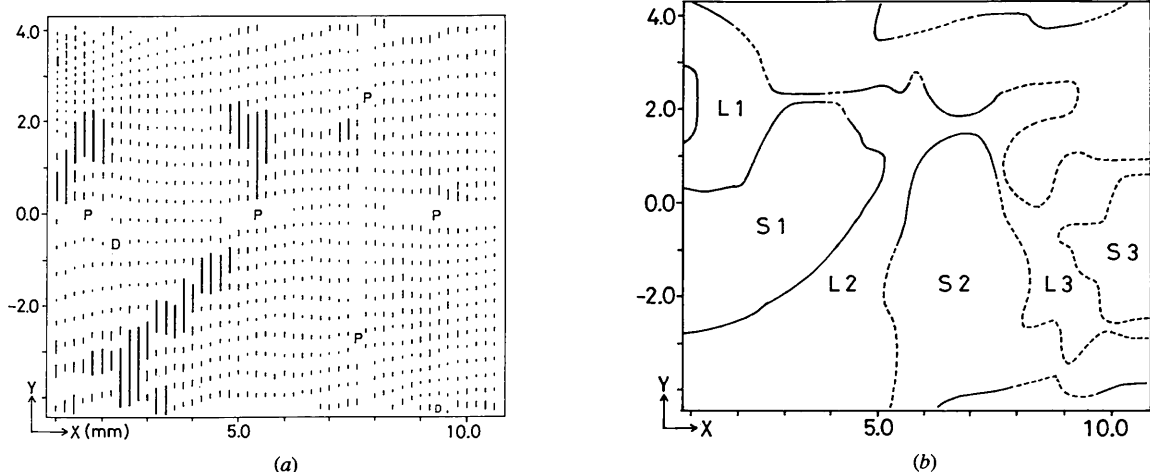

(a)

(b)

Fig. 9. (a) Amplitude distribution of the moiré-fringe oscillation determined over the whole field of the fringe pattern. T set no. 8, O-beam image. $r = 0.85$. For details see text. (b) Auxiliary contour map showing a feature of the amplitude distribution clearly. $L1$, $L2$ and $L3$ are large-amplitude areas ($a_M/\Lambda \geq 0.12$), while $S1$, $S2$ and $S3$ are small-amplitude areas ($a_M/\Lambda < 0.12$). Broken border lines mean that the demarcation involves some indistinctness because of a scatter in distributed amplitude.

in the topograph and in the amplitude map varies between the O and G images and among T sets under different pulling loads. These points will be reported in detail elsewhere.

4. Discussion and concluding remarks

In the following, we make some additional remarks and discussions on the results in the preceding section:

(a) It should be realized that moiré fringes' NPJ is not merely given as a graphical deformation of the fringe pattern but occurs as a wave–optical phenomenon in the wave field in space. Fringe profiles and their variations, complicated but methodical, can be produced by nothing other than a wave–optical effect. The moiré pattern varies as the variation of the interference pattern accompanying the phase variations of component waves. The explanation of the NPJ should take this character of the problem into consideration.

(b) In the manner of occurrence, the NPJ of moiré fringes may be featured by the oscillatory behavior of the fringes, irregularity or randomness of that oscillatory variation, and a partial regularity and coherence seen behind the general irregularity. It is interesting and important to consider on what basis or from what origin each of these features appears. Regarding the last point, the partial regularity has been observed in the variation of the fringe pattern (Fig. 3), fringe profiles (Figs. 4–6) and fringe slope plots (Fig. 8). Some degree and extent of spatial correlation or coherence has also been noted. The symmetric profile shapes (§3.2) found occasionally also represent a kind of regularity. The regularities thus found at different levels of inspection may be considered to be of one origin. They suggest that some structured methodical system with a wave–optical character operates at the basis of the phenomenon.

(c) The amplitude map in Fig. 9 may be considered as a figuration of such a methodical basis of the NPJ. The compared intensity patterns of the topographs would be understandable using the existing knowledge of X-ray diffraction. The amplitude map thus gives a good idea of how to elucidate the NPJ.

(d) The NPJ of moiré fringes has a slight resemblance to Fresnal diffraction in that the interference pattern varies along the optical axis. A comment should be made on the question of the relevance to Fresnel diffraction. Quantitatively, in the first place, the axial distances (z_d) from the specimen to the recorded moiré images are well within the effective range of Fresnal diffraction (Appendix D). However, the effective distance in the image plane is estimated of the order of 10 µm from the edge. This is below the resolution of images treated in the image processor. In addition, a representative value of the oscillation amplitude (a_M) of fringes is, say, 70 µm in the case of relatively large oscillations. Even amplitudes larger than 100 µm are not rare. Such magnitudes of displacement are too large to be produced by Fresnel

diffraction. Secondly, it must be emphasized that an opening or aperture to cause Fresnel diffraction is difficult to find in the present specimen. Even though point-like defects in the specimen as well as the black spot images from the collimator crystal (§3.1) would work as the aperture, they are distributed only at limited sites. They do not explain the fringe oscillation occurring over the whole field of the topographs. The weak lattice strain induced over the specimen (§2.1) does not matter with Fresnel diffraction. It is evident that the NPJ is not produced by Fresnel diffraction.

(d) It is still not known whether the condition $|K| = |K'|$, mentioned initially (§1), is broken down or not in the moiré-fringe interference. Although the breakdown of $|K| = |K'|$ would lead to the occurrence of NPJ, the converse does not necessarily hold. This question about $|K| = |K'|$ and the cause of the observed NPJ will be clarified step by step in future studies. Irrespective of the answer to the question, NPJ is an important property of moiré interference fringes.

APPENDIX A
Theory of moiré fringes

The moiré theory here is given by plane-wave diffraction theory, using Kato's theoretical form (see pp. 354–389 in Azaroff *et al.*, 1974). The theoretical framework and final results are essentially in accordance with previous treatments (Hashimoto, Mannami & Naiki, 1961; Simon & Authier, 1968).

Consider as specimen a bicrystal composed of parallel-sided crystals A and B having a reciprocal-lattice-vector difference Δg with a narrow gap between them. The dispersion-surface construction for this case is given in Fig. 10. For simplicity, the Lorentz point L is fixed instead of the origin of reciprocal space. An incident plane wave excites a transmitted and a diffracted wave (O and G waves, respectively), and each of the two waves excites again two partial waves in crystal B. Let these doubly excited waves be (O, O') and (O, G') waves and (G, O') and (G, G') waves. These waves, after emerging from crystal B, are given by

$$E_{oo'}(\mathbf{r}) = E_{oo'}(\mathbf{r}_{b'})\exp i\mathbf{K}_{oo'} \cdot \mathbf{r} \qquad (1a)$$

$$E_{og'}(\mathbf{r}) = E_{og'}(\mathbf{r}_{b'})\exp i\mathbf{K}_{og'} \cdot \mathbf{r} \qquad (1b)$$

$$E_{go'}(\mathbf{r}) = E_{go'}(\mathbf{r}_{b'})\exp i\mathbf{K}_{go'} \cdot \mathbf{r} \qquad (1c)$$

$$E_{gg'}(\mathbf{r}) = E_{gg'}(\mathbf{r}_{b'})\exp i\mathbf{K}_{gg'} \cdot \mathbf{r}. \qquad (1d)$$

Here, $\mathbf{r}$ is a position vector denoting an observation point behind the crystal and $\mathbf{r}_{b'}$ a position vector denoting the exit surface b'. Wave vectors $\mathbf{K}_{oo'}$, $\mathbf{K}_{og'}$ etc. are graphically represented in Fig. 10 as

$$\mathbf{K}_{oo'} = A\overrightarrow{_{oo'}O'}(=\overrightarrow{A_oO}), \quad \mathbf{K}_{og'} = A\overrightarrow{_{og'}G'},$$

$$\mathbf{K}_{go'} = A\overrightarrow{_{go'}O'}, \quad \mathbf{K}_{gg'} = A\overrightarrow{_{gg'}G'}(=\overrightarrow{A_gG}).$$

The moiré fringe interference occurs between (O, O') and (G, O') waves and between (O, G') and (G, G') waves. The corresponding wave-vector differences are

$$\Delta\mathbf{K}_o \equiv \mathbf{K}_{oo'} - \mathbf{K}_{go'} = 2\pi\Delta\mathbf{g} - [2\pi(\Delta\mathbf{g} \cdot \hat{\mathbf{K}}_o)/(\hat{\mathbf{K}}_o \cdot \mathbf{n})]\mathbf{n}$$
$$(2a)$$

$$\Delta\mathbf{K}_g \equiv \mathbf{K}_{og'} - \mathbf{K}_{gg'} = 2\pi\Delta\mathbf{g} - [2\pi(\Delta\mathbf{g} \cdot \hat{\mathbf{K}}_g)/(\hat{\mathbf{K}}_g \cdot \mathbf{n})]\mathbf{n}.$$
$$(2b)$$

Here, $\hat{\mathbf{K}}_o$ and $\hat{\mathbf{K}}_g$ denote unit vectors along the traveling direction of the O and G waves; $\mathbf{n}$ is the normal vector to the crystal surfaces. As is easily seen,

$$(\Delta\mathbf{K}_o \cdot \hat{\mathbf{K}}_o) = 0 \qquad (3a)$$

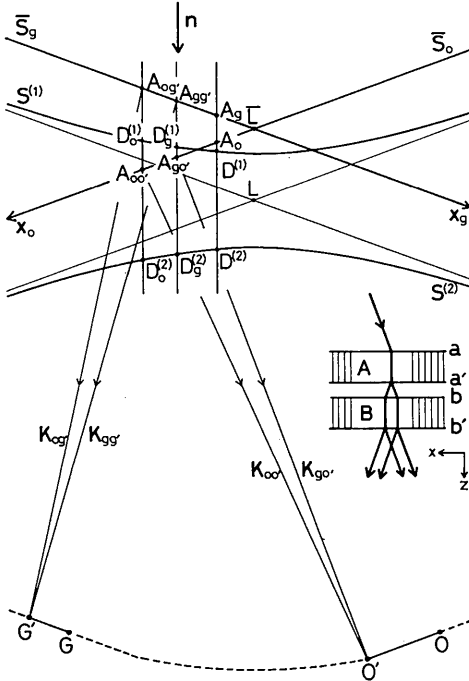$$(\Delta\mathbf{K}_g \cdot \hat{\mathbf{K}}_g) = 0. \qquad (3b)$$

Fig. 10. Dispersion-surface construction for a bicrystal with $\Delta\mathbf{g} \neq 0$. $D^{(1)}$, $D^{(2)}$ tie points for initially excited waves in crystal A; A_o, A_g wave points for vacuum waves incident upon crystal B; $D_o^{(1)}$, $D_o^{(2)}$, $D_g^{(1)}$, $D_g^{(2)}$ tie points of successively excited waves in crystal B; $A_{oo'}$, $A_{og'}$, $A_{go'}$, $A_{gg'}$ wave points of vacuum waves emerging from crystal B. (O, G) and (O', G') are reciprocal-lattice points in crystals A and B, respectively; $2\pi\Delta\mathbf{g} = \overrightarrow{O'G'} - \overrightarrow{OG}$.

Equations $(3a)$ and $(3b)$ correspond to the requirement that moiré fringes should be a projective image.

After performing an almost straightforward calculation, we obtain for the wave-field intensity at the observation point $\mathbf{r}$:

$$I_o(\mathbf{r}) = |\mathbf{E}_{oo'}(\mathbf{r}) + \mathbf{E}_{go'}(\mathbf{r})|^2$$
$$= I_{oo'} + I_{go'} + 2(I_{oo'}I_{go'})^{1/2}\cos\Psi_o(\mathbf{r}) \quad (4a)$$

$$I_g(\mathbf{r}) = |\mathbf{E}_{og'}(\mathbf{r}) + \mathbf{E}_{gg'}(\mathbf{r})|^2$$
$$= I_{og'} + I_{gg'} + 2(I_{og'}I_{gg'})^{1/2}\cos\Psi_g(\mathbf{r}) \quad (4b)$$

$$\Psi_o(\mathbf{r}) = \phi_{PO} + 2\pi[\Delta\mathbf{g} \cdot (\mathbf{r} - \mathbf{r}_o)] + K\alpha_{og}t_2 - (u_nt_{gap}/\gamma_g)$$
$$- 2\pi(\Delta\mathbf{g} \cdot \hat{\mathbf{K}}_o)(T_{b'}/\gamma_o) \quad (5a)$$

$$\Psi_g(\mathbf{r}) = \phi_{PG} + 2\pi[\Delta\mathbf{g} \cdot (\mathbf{r} - \mathbf{r}_o)] + K\alpha_{og}t_2 - (u_nt_{gap}/\gamma_g)$$
$$- 2\pi(\Delta\mathbf{g} \cdot \hat{\mathbf{K}}_g)(T_{b'}/\gamma_g) \quad (5b)$$

$$\phi_{PO} = -\tan^{-1}(B_o/A_o) \qquad (6a)$$

$$\phi_{PG} = -\tan^{-1}(B_g/A_g) \qquad (6b)$$

$$K\alpha_{og} = \tfrac{1}{2}(\Delta_o/\gamma_g - \Delta_g/\gamma_o)\sin 2\theta_B \qquad (7)$$

$$\Delta_o = -2\pi(\Delta\mathbf{g} \cdot \hat{\mathbf{K}}_g)/\sin 2\theta_B \qquad (8a)$$

$$\Delta_g = 2\pi(\Delta\mathbf{g} \cdot \hat{\mathbf{K}}_o)/\sin 2\theta_B \qquad (8b)$$

$$u_n = K\Delta\theta\sin 2\theta_B. \qquad (9)$$

Here, θ_B is the Bragg angle, K the wave number in vacuum, $\Delta\theta$ the deviation angle from the exact Bragg position; $\gamma_o = (\hat{\mathbf{K}}_o \cdot \mathbf{n})$ and $\gamma_g = (\hat{\mathbf{K}}_g \cdot \mathbf{n})$; $\mathbf{r}_o$ is a position vector of a point on the surface b such that Bravais-lattice points of crystals A and B coincide; t_2 is the thickness of crystal B, t_{gap} the width of the interspacing gap, $T_{b'} \equiv [\mathbf{n} \cdot (\mathbf{r} - \mathbf{r}_{b'})]$ the distance from the surface b' to the observation point; A_o, B_o and A_g, B_g are complicated functions of such parameters as $\Delta\theta$, $\Delta\mathbf{g}$, crystal thicknesses etc. and are related to the wave-field intensities so that $A_o^2 + B_o^2 = 4I_{oo'}I_{go'}$ and $A_g^2 + B_g^2 = 4I_{og'}I_{gg'}$; $I_{oo'}$ and $I_{go'}$ denote the intensities of (O, O') and (G, O') waves and $I_{og'}$ and $I_{gg'}$ the intensities of (O, G') and (G, G') waves. The intensities $I_{oo'}$, $I_{go'}$ etc. are determined on the exit surface b' and unvaried on emergence from the crystal, i.e. $I_{oo'} \equiv I_{oo'}(\mathbf{r}_{b'})$ etc.

Now, if we assume $(\mathbf{r} - \mathbf{r}_{b'}) \parallel \hat{\mathbf{K}}_o$ for the wave field $I_o(\mathbf{r})$, for example, it turns out that

$$2\pi[\Delta\mathbf{g} \cdot (\mathbf{r} - \mathbf{r}_{b'})] - 2\pi(\Delta\mathbf{g} \cdot \hat{\mathbf{K}}_o)(T_{b'}/\gamma_o) = 0.$$

Assuming symmetric Laue geometry $(\gamma_o = \gamma_g)$ in agreement with the experiment, we can show that

$$2\pi[\Delta\mathbf{g} \cdot (\mathbf{r}_{b'} - \mathbf{r}_o)] + K\alpha_{og}t_2 = 2\pi[\Delta\mathbf{g}_\parallel \cdot (\mathbf{r}_{b'} - \mathbf{r}_o)_\parallel],$$

where the symbol $\|$ denotes the component parallel to the crystal surface. Substituting these results into $(5a)$, we obtain

$$\Psi_o(\mathbf{r}) = \Psi_o(\mathbf{r}_{b'}) = \phi_{PO} + \phi_M + \phi_{gap} \quad (10a)$$

$$\Psi_g(\mathbf{r}) = \Psi_g(\mathbf{r}_{b'}) = \phi_{PG} + \phi_M + \phi_{gap} \quad (10b)$$

$$\phi_M = 2\pi[\Delta\mathbf{g}_\| \cdot (\mathbf{r}_{b'} - \mathbf{r}_o)_\|]$$
$$= (2\pi/d)[-(\Delta d/d)x_b + \Delta\rho y_b] \quad (11)$$

$$\phi_{gap} = -(u_n t_{gap}/\gamma_g). \quad (12)$$

Here, (x_b, y_b) is the coordinate taken on the surface b, d is the lattice spacing, Δd the difference in d and $\Delta\rho$ a relative rotation of the lattice plane about a horizontal axis. When ϕ_{PO}, ϕ_{PG} and ϕ_{gap} can be assumed constant, the fringe spacing and slope in the intensity field $I_o(\mathbf{r})$ or $I_g(\mathbf{r})$ are given respectively by

$$\Lambda = d/[(\Delta d/d)^2 + (\Delta\rho)^2]^{1/2} \quad (13a)$$

$$\tan\alpha_M = (\Delta d/d)/\Delta\rho. \quad (13b)$$

Phase terms (ϕ_{PO}, ϕ_{PG}), ϕ_M and ϕ_{gap} in $(10a,b)$ represent the contribution from the effects of extinction, $\Delta\mathbf{g}$ and the interspacing gap, respectively. The existence of ϕ_{gap} is verified experimentally for the case of $\Delta\mathbf{g} = 0$ (Yoshimura, 1991b). According to the formulation here, crystal moiré fringes are understood to be the pattern of phase variation $[2\pi\Delta\mathbf{g}_\| \cdot (\mathbf{r}_{b'} - \mathbf{r}_o)_\|]$, modulated by ϕ_{PO} or ϕ_{PG} and ϕ_{gap}. As is seen from $(4a,b)$ and $(10a,b)$, the wave-field intensity observed at $\mathbf{r}$ behind the crystal is always equal to the intensity at the corresponding emergence point $\mathbf{r}_{b'}$ on the surface b'. In other words, the observed image is a projection of $I_o(\mathbf{r}_{b'})$ or $I_g(\mathbf{r}_{b'})$.

APPENDIX B
Wavelength and angular spreads of the incident beam

The spectral window of the beam diffracted from the Si(220) collimator is represented by the hatched area in Fig. 11 (Nakayama, Hashizume, Miyoshi, Kikuta & Kohra, 1973). The angular width of the hatched (111) band is estimated to be $\omega = \omega_{s,111}b_1^{1/2}b_2 = 0.08''$; the angular spread in the whole wavelength range [i.e. the angular width of the (220) band] is $\omega_\Sigma = \omega_{s,220}b_2^{1/2} = 0.34''$ (Kikuta & Kohra, 1970). Here, $\omega_{s,111}$ and $\omega_{s,220}$ denote the angular widths (3.12 and 2.16'', respectively) for the symmetric diffraction and b_1 (= 1.0) and b_2 (= 1/40) the asymmetry factors for the 111 and 220 diffractions, respectively.

APPENDIX C
Supplements to the image processing

(a) The experiment of the D–E characteristic of single-coated X-ray films showed that the characteristic curve is given in the form of an empirical formula as follows:

$$D = 5.59[1 - \exp(-3.03E)] + 0.154, \quad (14)$$

where E denotes a relative exposure and 0.154 is the fog density.

(b) When an image is input into the image processor with linear presetting, the intensity or transmitted luminance of the input image is given by

$$I(X,Y) = I_o(X,Y)10^{-D(X,Y)}, \quad (15)$$

where $I_o(X,Y)$ denotes the incident illumination and $D(X,Y)$ the film density. By transforming $I(X,Y)$ and $I_o(X,Y)$ into logarithmic form in the image processor, the D value is obtained as follows:

$$D(X,Y) = [I_o^{\log}(X,Y) - I^{\log}(X,Y)]/105.9 \quad (16)$$

$$I_o^{\log}(X,Y) = 255\log_e[I_o(X,Y) + 1]/\log_e(255 + 1) \quad (17a)$$

$$I^{\log}(X,Y) = 255\log_e[I(X,Y) + 1]/\log_e(255 + 1). \quad (17b)$$

Here, $I_o^{\log}(X,Y)$ and $I^{\log}(X,Y)$ are the logarithm-transformed images of $I_o(X,Y)$ and $I(X,Y)$. This D value was corrected to the true value by calibrating with the microphotometric D value. (The calibration curve was $D_m = 0.048 + 1.052D_p - 0.271D_p^2$, D_m and D_p being the microphotometric and image-processor D values, respectively.)
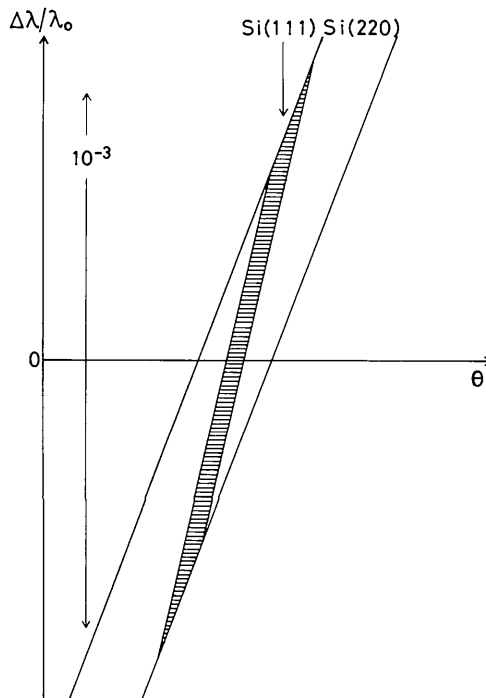

Fig. 11. DuMond's diagram for the Si(111) and (220) monochromator–collimator system in Fig. 1. The slopes of the bands (111) and (220) are arbitrary.

(c) The incident illumination had a nonuniformity as does the background density below the oscillatory part in the moiré topographs. These two nonuniformities were much more slowly varying than the oscillatory density variation of moiré fringes. The nonuniformity in the input image owing to the two nonuniformities above were flattened by the shading correction and only the oscillatory variation corresponding to fringes remained. The image intensity after receiving gray-level reversal and dynamic range expansion following the shading correction can be written with a good accuracy as

$$I(X,Y) = I_c + \Delta I\{2.3\Delta D(X,Y) - 2.65[\Delta D(X,Y)]^2$$
$$+ 2.03[\Delta D(X,Y)]^3 - \ldots\}, \qquad (18)$$

where I_c and ΔI are constants and $\Delta D(X,Y)$ represents the oscillatory part of the density corresponding to the fringes.

APPENDIX D
Note on the effective distance of Fresnel diffraction

The effective range of Fresnel diffraction along the optical axis is estimated by

$$f < a^2/\lambda \qquad (19)$$

(e.g. Kubota, 1971), where f, a and λ represent the object-to-image-plane distance, aperture size and wavelength, respectively. If we assume $a = 10\,\mu m$ as an appropriate minimum value, substitution into (19) gives $f < 1.4\,m$.

The effective distance in the image plane, ΔY, may be estimated from Fresnel's integral by

$$\Delta Y < (\lambda f/2)^{1/2}v. \qquad (20)$$

Here, v means the argument in Fresnel's integral. If we assume $f = 60\,mm$ and $v = 10$ as a reasonable maximum, substitution into (20) gives $\Delta Y < 15\,\mu m$.

References

Azaroff, L. V., Kaplow, R., Kato, N., Weiss, R. J., Wilson, A. J. C. & Young, R. A. (1974). X-ray Diffraction, pp. 176–438. New York: McGraw-Hill.
Hart, M. (1972). Philos. Mag. 26, 821–831.
Hashimoto, H., Mannami, M. & Naiki, T. (1961). Philos. Trans. R. Soc. London Ser. A, 253, 490–516.
Ishikawa, T. (1990). J. Cryst. Growth, 103, 131–140.
Kikuta, S. & Kohra, K. (1970). J. Phys. Soc. Jpn, 29, 1322–1328.
Kubota, M. (1971). Hado Kogaku (Wave Optics). Tokyo: Iwanami. (In Japanese.)
Lang, A. R. (1968). Nature (London), 220, 652–657.
Nakayama, K., Hashizume, H., Miyoshi, A., Kikuta, S. & Kohra, K. (1973). Z. Naturforsch. Teil A, 28, 632–638.
Simon, D. & Authier, A. (1968). Acta Cryst. A24, 527–534.
Yoshimura, J. (1987). Acta Cryst. A43, C221.
Yoshimura, J. (1989). J. Phys. Soc. Jpn, 58, 1283–1295.
Yoshimura, J. (1991a). Acta Cryst. A47, 139–142.
Yoshimura, J. (1991b). Phys. Status Solidi A, 125, 429–440.
Yoshimura, J. (1992). J. Crystallogr. Soc. Jpn, 34, 19–26. (In Japanese.)
Yoshimura, J. & Ishikawa, T. (1990). Acta Cryst. A46, C424–C425.